Critical behavior and phase diagram of layered ferromagnetic FeTa$_3$S$_6$ single crystals

Azizur Rahman,[1,2,*] Majeed Ur Rehman,[3,*] Maryam Kiani [ORCID],[3] Hongze Zhao,[1] Jianlin Wang,[4,5] Yalin Lu,[4,5] Keqing Ruan,[1,6] Rucheng Dai,[7] Zhongping Wang [ORCID],[7] Lei Zhang,[2] Jian Wang,[3,†] and Zengming Zhang [ORCID][7,6,‡]

[1]*Department of Physics, University of Science and Technology of China, Hefei 230026, China*
[2]*High Magnetic Field Laboratory, Hefei Institutes of Physical Science, Chinese Academy of Sciences, Hefei 230031, China*
[3]*College of Physics and Optoelectronic Engineering, Shenzhen University, Nanhai Ave 3688, Shenzhen, Guangdong 518060, China*
[4]*Hefei National Laboratory for Physical Sciences at the Microscale, University of Science and Technology of China, Hefei 230026, China*
[5]*Anhui Laboratory of Advanced Photon Sciences and Technology, University of Science and Technology of China, Hefei 230026, China*
[6]*Key Laboratory of Strongly-Coupled Quantum Matter Physics, Chinese Academy of Sciences, School of Physical Sciences, University of Science and Technology of China, Hefei, Anhui 230026, China*
[7]*The Centre for Physical Experiments, University of Science and Technology of China, Hefei 230026, China*

The magnetization of the highly air-stable two-dimensional (2D) intrinsic ferromagnet FeTa$_3$S$_6$ single crystal has been systematically investigated. Magnetization measurement revealed paramagnetic to ferromagnetic (PM-FM) phase transition at around 35 K and a strong magnetic anisotropy along the crystallographic c axis ($H \parallel c$). The critical exponents $\beta = 0.189(2)$, $\gamma = 1.423(1)$, and $\delta = 8.531(7)$ with $T_c = 35$ K suggest that the spin interaction of a two-dimensional (2D) Ising type in FeTa$_3$S$_6$ coupled with long-range ($\sigma = 1.581$) interaction. A comprehensive magnetic phase diagram based on detailed magnetization measurements and universality scaling of FeTa$_3$S$_6$ is constructed over three magnetic field regions. The magnetic phase diagram of FeTa$_3$S$_6$ is analogous to that of CrNb$_3$S$_6$, which exhibits a chiral magnetic soliton lattice. DFT simulation reveals that the large magnetic anisotropy energy in FeTa$_3$S$_6$ originates from the combined effects such as considerable orbital magnetic moment, host lattice spin-orbit coupling, and hybridization between host lattice $2H - \text{TaS}_2$ and the intercalated Fe component. Furthermore, the magnetic anisotropy ($\parallel c$) in FeTa$_3$S$_6$ is due to the dominant contribution of the spin conserving process $\Delta S_z = 0$ in magnetic anisotropy energy, which differs from that of CrNb$_3$S$_6$, or MnNb$_3$S$_6$, where the spin flipping process $\Delta S_z = 1$ dominates, causing in-plane ($\perp$ c) magnetic anisotropy.

I. INTRODUCTION

Two-dimensional (2D) materials have recently stimulated significant interest in the development of novel properties and potential applications [1–5]. Most of the 2D materials are nonmagnetic or antiferromagnetic by nature. Therefore, 2D ferromagnetic (FM) materials are of great importance to boost next-generation spintronic devices [6–11]. To explore 2D magnetism, layered or quasilayered materials are preferred over nonlayered magnets because they can be downsized to one or two layers without compromising the sample's ferromagnetic nature [12]. Very recently, many efforts have been devoted towards this novel direction. For instance, CrI$_3$ [13–17], Cr$_2$Ge$_2$Te$_6$ [4,16], Cr$_2$Si$_2$Te$_6$, and Fe$_3$GeTe$_2$ [17,18] are the layered materials that exhibit the 2D ferromagnetism in bulk as well as nanosheets form, even to a single layer. However, there are still many challenges and issues, including poor stability and lower Curie temperatures going from the bulk to the thinner geometry, i.e., quasi-2D structure, hampering the experimental investigation of intrinsic

2D ferromagnetism and technological applications [17,19]. For example, CrI$_3$ nanosheet degrades in the air in 15 minutes, Fe$_3$GeTe$_2$ nanosheet ferromagnetism disappears under the atmosphere for a few hours [17,19], and Cr$_2$Si$_2$Te$_6$ has a low Curie temperature. Similarly, a weak ferromagnetic signal is observed in a few layers of the Cr$_2$Ge$_2$Te$_6$ sample using the magneto-optical Kerr effect (MOKE) [20]. The magnetism strongly depends on the number of layers and T_c drops to a very lower temperature for bi- or trilayers sample of Cr$_2$Ge$_2$Te$_6$ [12]. T_c was also found to be unexpectedly dependent on the external magnetic field in the 2D limit compared to its bulk form [12]. The discrepancies found in the 2D limit are due to the fundamental difference between 2D and 3D materials, i.e., in bulk materials, the transition to a ferromagnetic state is driven by the exchange interactions among spins and their neighbors, while in 2D, the exchange of interactions alone cannot generate magnetic order; the governing factor is magnetic anisotropy [21]. And the magnetic anisotropy of Cr$_2$Ge$_2$Te$_6$ is moderate ($\sim$1T). CrI$_3$ has a similar T_c to Cr$_2$Ge$_2$Te$_6$, 61 K and its comparatively large magnetic anisotropy ($\sim$3T) is well suited for the investigation of 2D ferromagnetism. The MOKE signal from CrI$_3$ is orders of magnitude greater than the that signal from Cr$_2$Ge$_2$Te$_6$ [22]. However, CrI$_3$ has a considerable disadvantage of being unstable, as we discussed earlier.

*These authors contributed equally to this work.
†Corresponding author: jianwang@hku.hk
‡Corresponding author: zzm@ustc.edu.cn

The exploration of 2D ferromagnetism thus requires a highly stable layered ferromagnetic material with a strong magnetic anisotropy. In this sense, very recently, Fe-intercalated transition metal dichalcogenides (TMDCs), TaS_2, labeled as $FeTa_3S_6$, has been noticed as a two-dimensional ferromagnetic material [23]. Intrinsic few-layer ferromagnetism in $FeTa_3S_6$ is identified by polar magneto-optical Kerr effect measurement that demonstrates a giant MOKE response. In addition to considerable out-of-plane ferromagnetism that survives down to a few layers, $FeTa_3S_6$ has an increasing trend of T_c by reducing it from bulk to 2D. More importantly, $FeTa_3S_6$ has excellent air stability and high magneto-crystalline anisotropy, making it the perfect platform for the investigating of 2D magnetism. In order to explain the magnetic behavior of the few-layer samples and the future application of this material, it is necessary to determine the nature of the magnetism in the bulk. In this paper, we present a comprehensive and detailed magnetic study by combining experiments with first-principles calculations on Fe-intercalated into TaS_2, $FeTa_3S_6$ single crystals.

II. RESULTS AND DISCUSSION

A. Methods

$FeTa_3S_6$ single crystals were grown using a solid-state reaction and chemical vapor transport method. High purity iron powders (99.5%), tantalum powders (99.999%), and sulfur (99.999%) were weighed and mixed at a ratio of 0.4:1:2 [24] and appropriate iodine as transport agents and then sealed under vacuum in a quartz tube. Quartz tubes were placed into a chamber furnace for solid-state reaction and held at 1323 K for 3 days. Whereafter, quartz tubes were placed in a two-zone furnace for the chemical vapor transport method. The prereaction was carried out by reverse transport for 3 days, then the source was maintained at 1253 K and the sink was maintained at 1153 K for another 7 days. The structure and phase purity of the $FeTa_3S_6$ were characterized by x-ray diffraction (XRD) (Rigaku SmartLab) with Cu K_α radiation. The magnetizations of the samples were measured by SQUID-VSM (Quantum Design, USA). The magnetic field was applied in no-overshoot mode and relaxed for 2 min before data collection to ensure an accurate magnetic field and data. In particular, when the initial isothermal magnetization was measured, the sample was cooled to the desired temperature under zero magnetic field after being sufficiently heated for 10 min above T_c.

For the DFT calculations, we use the pseudopotential approach in the framework of the so-called projected augmented-wave (PAW) method [25] as implemented in the Vienna *ab initio* simulation package (VASP) [26]. To describe the exchange-correlation interaction, the GGA-PBE scheme was chosen [27]. All the degrees of freedom were relaxed until the Hellmann- Feynman force on each component is lower than –0.01 eV/Å. The Monkhorst-Packgrid of 17 × 17 × 7 centered around the Γ point was chosen to sample the BZ. For the expansion of the plane waves, a basis set with the cutoff energy of 520 eV was taken. To address the strong correlation effects as important in the case of $3d$ magnetic components, we use the so-called GGA+U potential [28]
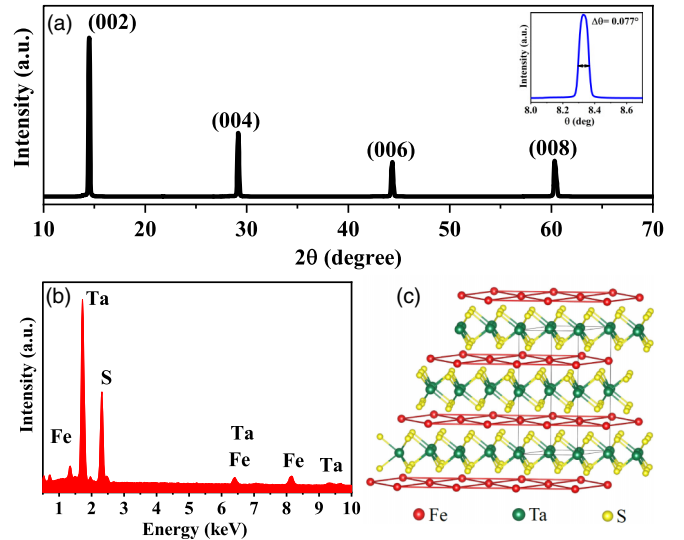

FIG. 1. (a) Single crystal XRD pattern of $FeTa_3S_6$ at room temperature. The observed sharp $(0, 0, l)$ peaks imply the high quality of $FeTa_3S_6$ single crystal [the x-ray rocking curves from the reflection of (002) peak]. (b) A typical EDX spectrum for single-crystal $FeTa_3S_6$. (c) The crystal structure of $FeTa_3S_6$, which consists of alternate stacking of TaS_2 layers where the Fe atoms are intercalated between TaS_2 layers (a side view).

with the Hubbard parameter U = 4.5 and exchange energy parameter $J = 0.7$ eV [29]. To cover the van der Waals (Vdw) interaction between the adjacent layers, we included the DFT-D_3 method of Grime [30]. For the 2D sheets, a slab model was used with vacuum thickness around 20 Å.

B. Structural properties

Figure 1 shows the structure information of $FeTa_3S_6$. Figure 1(a) shows the single-crystal XRD pattern, only (00*l*) peaks were observed, suggesting that the surface of the crystal is normal to the *c* axis with the plate-shaped surface parallel to the ab plane. A series of strong sharp diffraction peaks are consistent with the previous paper [23] and (JCPDS No. 22-0360), demonstrating high crystalline quality and layered features of the as grown $FeTa_3S_6$ single crystals. The chemical ratio was determined by the EDX spectrum as displayed in Fig. 1(b), which shows that the Fe:Ta:S ratio is close to 1:3:6. The quality of the grown $FeTa_3S_6$ single crystals is further confirmed by measuring rocking curves. The x-ray rocking curves from the reflection of (002) show that the full widths of the rocking curves at half-maximum (FWHM) are 0.077 as shown in the inset of Fig. 1(a). The single peak and narrow FWHM of the rocking curve show the high quality of a single crystal sample with no misoriented blocks or twin crystal. Figure 1(c) illustrates the structural schematic diagram of $FeTa_3S_6$, which crystallizes in a hexagonal layered lattice structure that is alternately stacked with Fe atoms and H-phase TaS_2 layers with the space group of $P6_322$ (No. 182) [23].

C. Magnetization

Figure 2(a) shows the temperature dependent magnetization $M(T)$ for applied magnetic fields $H \parallel c$ and $H \perp c$ with
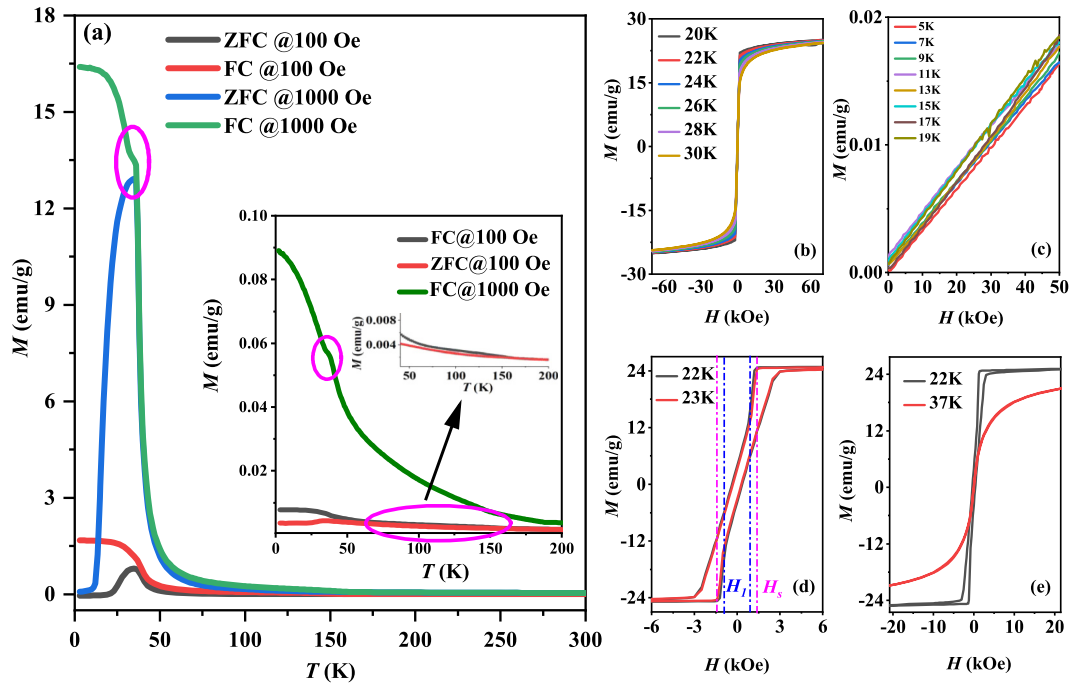
FIG. 2. (a) Temperature dependence of magnetization $M(T)$ measured at 100 Oe and 1000 Oe along the crystallographic c axis $H \parallel c$. The purple circle is drawn to indicate the characteristic kink (discussed in the text). The inset shows the field dependence of magnetization $M(T)$ measured for $H \perp c$. (b) Isothermal magnetization as a function of applied field $M(H)$ at selected temperatures with $H \parallel c$ (c) $H \perp c$ (d) the magnified $M(H)$ in the low-field regions to clearly show the magnetic steps. The blue- and purple-dotted lines are drawn to estimate field that induced phase transition (from P_1 to P_2) and saturation magnetization for FM phase (P_3), respectively at specific temperatures. (e) $M(H)$ loops at T = 22 K (below T_c) and 37 K (just above T_c) are shown. The unusual behavior (magnetic steps) disappears above T_c.

a zero field cooled (ZFC) and field cooled (FC) protocols. As the temperature decreases, there is a sharp increase in each $M(T)$ curve, indicating a ferromagnetic phase transition. A sharp kink occurs in the $M(T)$ curve at the onset of the magnetic phase transition under the magnetic field of 1000 Oe applied along the c axis. The phase transition temperature (T_c) was estimated to be 36 K, determined from the kink on the $M(T)$ curve. The separation of the $M(T)$ curve between ZFC and FC appears at high temperature ($\sim$160 K), which could be due to magnetic disorders caused by atomic disorders or could indicate the presence of a small amount of $FeTa_4S_8$ ($T_c \sim$ 160 K) [31,32] phase as an impurity. The kink like behavior in the $M(T)$ curve in the lower-field region usually implies hint for helimagnetic ordering, as seen in isostructural compounds such as $CrNb_3S_6$ [33] and $MnNb_3S_6$ [34]. $FeTa_3S_6$ has been confirmed as a chiral magnet in the MTa_3S_6 (M = Cr, Mn, Fe, Co, and Ni) family [35,36]. Additionally, Fe ($FeTa_3S_6$) has a high SOC than Cr ($CrNb_3S_6$) and Mn ($MnNb_3S_6$) due to its sizable atomic number Z [37]. The chirality with high spin-orbital coupling in the crystal structure of $FeTa_3S_6$ results in an antisymmetric exchange interaction called the Dzyaloshinskii-Moriya (DM) interaction [38]. Therefore, the novel magnetic ground state established by competing DM interactions with ferromagnetic coupling is also highly anticipated in $FeTa_3S_6$.

Figures 2(b) and 2(c) display the isothermal magnetization $M(H)$ loops measured at different temperatures for $H \parallel c$ and $H \perp c$, respectively. All $M(H)$ curves below T_c for $H \parallel c$

exhibit saturation and are ferromagnetic in nature, whereas, the magnetization increases linearly with applied field for the $M(H)$ curves measured along $H \perp c$, indicating the magnetization easy axis along $H \parallel c$. The saturation magnetization is estimated to be $\sim$4.03 $\mu_B/f.u.$, indicating that Fe in the $FeTa_3S_6$ is in the form of Fe^{+2}. The magnetization arises mainly from the unpaired electrons of the intercalated atoms (Fe) in the $FeTa_3S_6$.

Two symmetrical magnetic steps in the low-field region before saturation can be noticed in $M(H)$ curves for $H \parallel c$ and are distinct from those of typical ferromagnetic materials. The two noticeable magnetic reflection points refer to the two distinct magnetic phases separated by the applied magnetic field as shown in Fig. 2(d). This shows that when the magnetic field increases, the modulated magnetic state initially transforms into an intermediate phase and eventually polarizes into an FM phase. Furthermore, the $M(H)$ curve shows a clear hysteresis loop below T_c. While, the width of the loop (ΔH) shrinks at an increasing temperature and finally disappears above T_c as shown in Fig. 2(e). This phenomenon has been seen in $CrNb_3S_6$ (isostructural to $FeTa_3S_6$) where the intermediate phase (between HM and FM phase) is identified as chiral soliton lattice (CSL) [33]. Evidence for CSL has been seen in magnetization and transport measurement for other intercalant TMDCs but has been convincingly confirmed in $CrNb_3S_6$ to date [39,40]. Latest reports on this theme include a single neutron diffraction analysis of polycrystalline $CrTa_3S_6$ [41] and several magnetization and diffraction studies of $MnNb_3S_6$ [34,42,43], which indicated that these materials could be
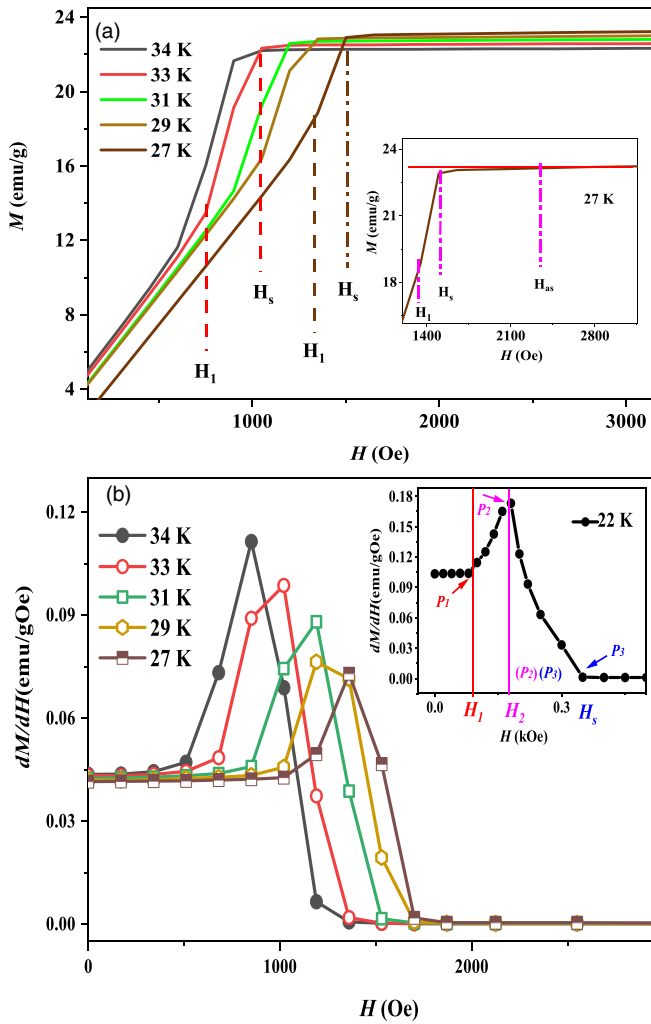
FIG. 3. (a) Initial magnetization isotherms $M(H)$ below T_c from T = 14 K to T = 34 K with $H \parallel c$ (b) $d[M(H)]/dH$ curves from 14 K to 34 K with $H \parallel c$ (definitions of H_1, H_2, and H_s are discussed in the text). The inset is the magnified $d[M(H)]/dH$ curves at T= 22 K in the low-field region. The magnetic field induced phase separation regions are marked as P_1, P_2, and P_3. The region marked with ($P_2 P_3$) is the region with coexistence of two phases P_1 and P_2. P_2 is dominant at low fields and P_3 is dominant at high field.

the next chiral soliton lattice candidates. In this context, the findings in this paper firmly establish the ferromagnetic intercalated TMDC compound, FeTa$_3$S$_6$ as a strong candidates for hosting exotic magnetic phases and motivate further work.

In order to accurately estimate field-induced transition points, magnetic isotherms [$M(H)$] were measured around T_c in low field as shown in Fig. 3(a). At low fields, the inflection points (H_1 and H_s) can be seen clearly. The [$M(H)$] curves appear to be saturated at critical fields H_s, but a closer look [see inset of Fig. 3(a)] reveals that the actual saturation occurs at relatively high fields (H_{as}). Therefore, the relatively accurate critical fields are estimated using $d[M(H)]/dH$ curves. Figure 3(b) shows $d[M(H)]/dH$ in a temperature range below T_c. Three distinct regions are found on the $d[M(H)]/dH$ curve, a plateau in a low-field region followed by a peak and drops to very low values as the field rises. Three inflection points
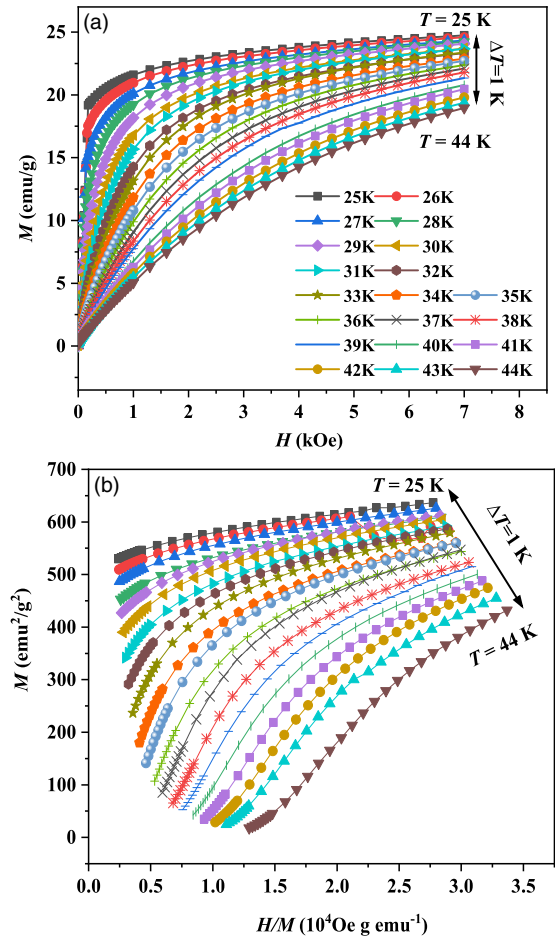

FIG. 4. (a) The initial isothermal magnetization curves around T_c; (b) Arrott plot of H/M vs M^2 around T_c.

are marked as H_1, H_2, and H_s, referring to the field induced phase transition points. Two inflection points H_1 and H_s have already been found in the $M(H)$ curves below T_c, while H_2 is a new finding in this $d[M(H)]/dH$ curve analysis. This shows that the FeTa$_3$S$_6$ single crystalline system undergoes two intermediate phases at H_1 and H_2 and ultimately to FM at H_s from HM ground state by changing the external magnetic field. The inset of Fig. 3(b) shows the $d[M(H)]/dH$ curve at 22 K where all the inflection points H_1, H_2, and H_s are marked. The scheme of phase transition observed and the nature of the phases will be discussed in the next sections.

D. Critical exponents analysis

Figure 4(a) shows all the magnetic isotherms $M(H)$ at high fields around T_c for $H \parallel c$. Based on these $M(H)$ curves, the Arrott plot was constructed assuming critical exponents following the mean-field theory with $\beta = 0.5$ and $\gamma = 1$ as shown in Fig. 4(b). All the lines in this plot show a nonlinear behavior having a downward curvature even in the high-field region. This means that the magnetic interaction in FeTa$_3$S$_6$ can not be described by conventional Landau mean-field model. Moreover, the order of the magnetic phase transition can be estimated through the slope of straight line according to Banerjee's criterion [44]: A positive slope refers to second order while negative slope corresponds to first-order phase
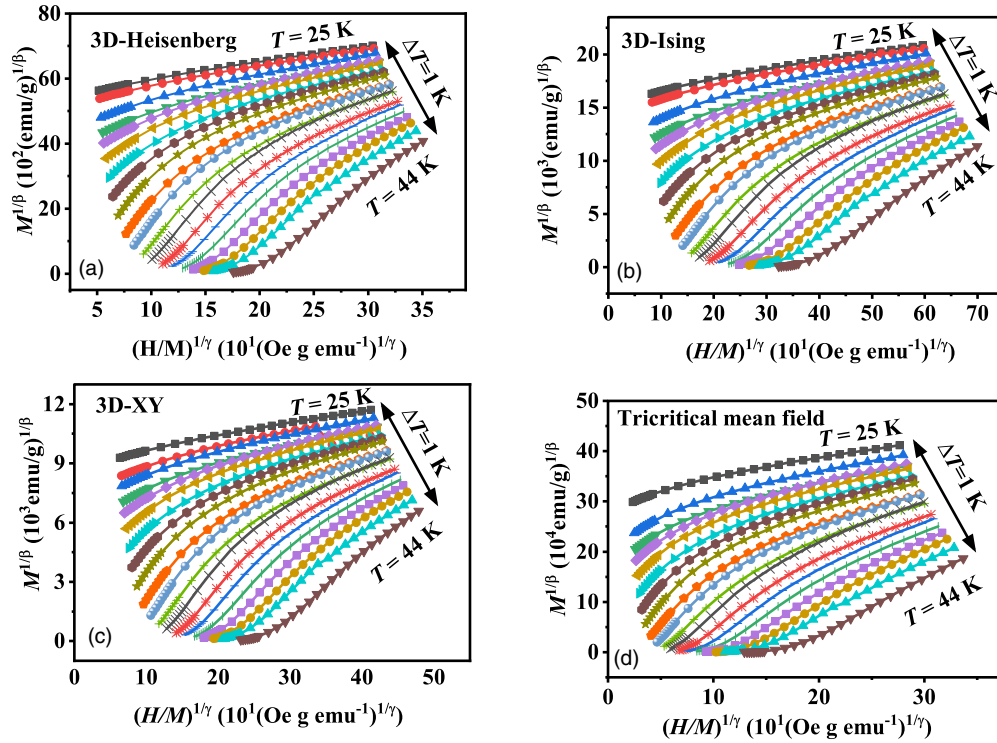
FIG. 5. The isotherms plotted as $M^{1/\beta}$ vs $(H/M)^{1/\gamma}$ with a (a) 3D Heisenberg model, (b) 3D Ising model, (c) 3D XY model, and (d) tricritical mean-field model.

transition. Therefore, the positive slope of the M^2 vs H/M curves shows that the order of phase transition in FeTa$_3$S$_6$ is the second order.

The second-order phase transition around T_c shows the critical behavior of the various thermodynamic variables, governed by critical fluctuations. The critical behavior is characterized by a set of interrelated statistical parameters, such as β, γ, and δ. The parameters β (associated with spontaneous magnetization below T_c), γ (associated with inverse magnetic susceptibility above T_c), and δ (associated with T_c) are critical exponents. From magnetization measurements, the above mentioned exponents are mathematically described as follows [45]:

$$M_S(T) = M_0(-\varepsilon)^\beta, \varepsilon < 0, \tag{1}$$

$$\chi_0^{-1}(T) = (h_0/M_0)(\varepsilon)^\gamma, \varepsilon > 0, \tag{2}$$

$$M = DH^{1/\delta}, \quad \varepsilon = 0, \quad [T = T_c] \tag{3}$$

where $\epsilon = (T - T_c)/T_c$ is the reduced temperature and h_0/M_0 and D are critical amplitudes. The critical behavior in the vicinity of T_c can be described by a series of critical exponents that follow the Arrott-Noakes equation of state in the critical region [46]:

$$(H/M)^{1/\gamma} = (T - T_c)/T_c + (M/M_1)^{1/\beta} \tag{4}$$

where M_1 is constant. Critical exponents provide important clues, such as the nature of spin interaction, spin dimensionality, and decaying length of magnetic coupling. Four sets of critical exponents corresponding to 3D-Heisenberg model ($\beta = 0.365$, $\gamma = 1.386$), 3D XY ($\beta = 0.345$, $\gamma = 1.316$), 3D Ising model ($\beta = 0.325$, $\gamma = 1.24$), and tricritical mean-field

model ($\beta = 0.25$, $\gamma = 1.0$) [44] were tested to construct Arrott plots. As shown in Figs. 5(a)–5(d) all the models failed to produce straight lines, suggesting that all these 3D models are not suitable for FeTa$_3$S$_6$.

Considering the strong 2D characteristics in FeTa$_3$S$_6$, the isothermal magnetization data in the critical region was further analyzed with 2D Ising model ($\beta = 0.125$, $\gamma = 1.75$). The corresponding plot is presented in Fig. 6(a) that shows a set of quasistraightlines. However, no straight line passes through the origin, showing that the FeTa$_3$S$_6$ system cannot be rigorously explained by the 2D Ising model. Therefore, the critical exponents need to be modified under the framework of 2D Ising model in order to obtain the precise value of T_c. To find out the proper values of critical exponents (β and γ) as well as T_c, the magnetization was reanalyzed using the modified Arrott plot analysis using Eq. (4). A rigorous iterative method has been adopted to avoid nonphysical fittings as well as systematic errors in the exponent values [47]. The starting values of χ_0^{-1}(T) and $M_s(T)$ were determined from the Arrott plot constructed following 2D Ising model shown in Fig. 6(a) by the linear extrapolation of the magnetic isotherms from high-field regions to the intercepts with the axis $(H/M)^{1/\gamma}$ and $M^{1/\beta}$, respectively. New values of β and γ can be determined by fitting the data following Eqs. (1) and (2). Using these new values of these exponents, the modified Arrott plot was constructed similar to the one shown in Fig. 6(a). This process was repeated until the stable values of β and γ were obtained. Following this procedure, the critical exponents obtained hardly depend on the initial parameters, which confirm the reliability and the intrinsic nature of these exponents. Figure 6(b) shows the final modified Arrott plot, constructed with the exponents values $\beta = 0.189(2)$ and $\gamma = 1.423(1)$. It
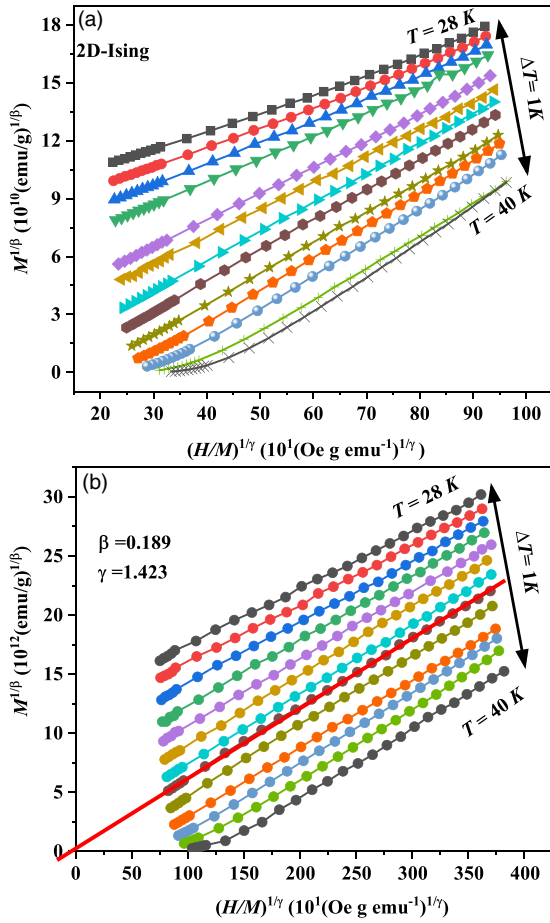
FIG. 6. (a) 2D Ising model plot of isotherms for $FeTa_3S_6$. (b) Modified Arrott plot of $M^{1/\beta}$ vs $(H/M)^{1/\gamma}$ with $\beta = 0.189$ and $\gamma = 1.423$ for $FeTa_3S_6$. The straight line is the linear fit of the isotherm at T = 35 K.

is clear from final modified Arrott plot that all the lines are very straight in the high-field region and a line passes through origin at T_c= 35 K.

Figure 7(a) shows the finally obtained $M_s(T)$ and $\chi_0^{-1}(T)$ values with solid fitting curves following Eqs. (1) and (2). The fitting result yield $\beta = 0.189(2)$ with $T_c = 35.2$ K and $\gamma = 1.423(1)$ with $T_c = 34.8$ K. The values obtained here are in agreement with those obtained using modified Arrott plot analysis. Figure 7(b) shows the magnetic isotherm $M(H)$ at the critical temperature $T_c = 35$ K in log-log scale. The $M(H)$ curve at T_c shows a straight line on the log-log scale when $H > H_s$. Thus, following Eq. (3) the third critical exponent $\delta = 8.471(7)$ can be determined in the high-field region ($H > H_s$). Alternatively, the exponent δ can be obtained from the Widom scaling law [48], according to which these exponents must fulfill the following relationship:

$$\delta = 1 + \frac{\gamma}{\beta}. \tag{5}$$

Following Eq. (5) and using the values of β and γ obtained from the modified Arrott plot analysis, $\delta = 8.531(7)$ was calculated, which is consistent with the value obtained from the critical isotherm analysis. This indicates that the estimated values are self consistent and reliable. All the critical expo-
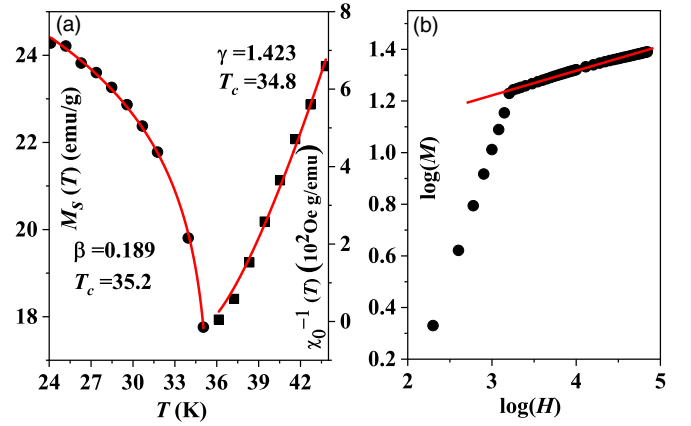

FIG. 7. (a) The spontaneous magnetization M_s (left) and inverse initial susceptibility χ_0^{-1} (right) vs T with the fitting solid curves; (b) The field dependence of the magnetization isotherm at T_c= 35 K for $FeTa_3S_6$ on a ln-ln scale, where the solid line is the linear fit following Eq. (S3) [37] that gives the critical exponent δ.

nents obtained in this work for $FeTa_3S_6$ are listed in Table I along with the values of other helimagnetic materials and theoretically predicted for various models. The magnetic coupling in $FeTa_3S_6$ is 2D type, but unlike its sister compounds, such as $CrNb_3S_6$ and $MnNb_3S_6$, which have 3D type magnetic coupling. This is due to the fact that spins in $FeTa_3S_6$ are mainly coupled within the *ab* plane. However, the deviation of the experimentally determined values from the theoretically predicted values of the 2D Ising model is due to the nonnegligible interlayer coupling owing to the ionic bonding effect between the Fe atoms and the TaS_2 layers.

Furthermore, the effective exponents β_{eff} and γ_{eff} are obtained by Eq. (6) for $FeTa_3S_6$ to clarify whether the determined critical exponents belong to any universality class in the asymptotic region:

$$\beta_{\text{eff}}(\varepsilon) = \frac{d[\ln M_s(\varepsilon)]}{d(\ln \varepsilon)}, \quad \gamma_{\text{eff}}(\varepsilon) = \frac{d[\ln \chi_0^{-1}(\varepsilon)]}{d(\ln \varepsilon)}. \tag{6}$$

The β_{eff} and γ_{eff} as a function of reduced temperature ϵ are plotted in Fig. 8. β_{eff} ($T < Tc$) shows a nonmonotonic variation with ϵ. Whereas, γ_{eff} ($T > Tc$) shows monotonic variation with ϵ, and converges when the temperature approaches T_c, defining the universality class to be 2D Ising model. However, nonmonotonic changes are attributed to magnetic disorders or the presence of $FeTa_4S_8$ because crystal growth via chemical vapor transport frequently encounters difficulties in controlling the amount of elements, which must be very small, which is beyond the XRD accuracy limit. As previously stated, the branching of the $M(T)$ curves under the ZFC and FC at around 160 K implies the presence of magnetic disorders or small amount of $FeTa_4S_8$, which is consistent with the conclusion achieved here. For a second-order phase transition, the critical exponents for a homogeneous magnet should be independent of the microscopic details of the system due to the divergence of correlation length in the vicinity of the transition point [49,50]. Hence, the critical exponents obtained here and the nonmonotonic changes of β_{eff} ($T < Tc$) and convergence of both γ_{eff} ($T > Tc$) and β_{eff} are intrinsic.

TABLE I. Comparison of critical exponents of FeTa$_3$S$_6$ with different theoretical models. MAP, modified Arrott plot; KF, Kouvel-Fisher method; CI, critical isotherm analysis.

Composition	References	Technique	β	γ	δ
FeTa$_3$S$_6$	This paper	MAP	0.189(2) (3)	1.423(1)	8.531(7)
CrNb$_3$S$_6$	[33]	MAP	0.370(4)	1.380(2)	4.853(6)
MnNb$_3$S$_6$	[34]	MEC	0.3681(1)	1.3917(2)	4.7805(7)
MnSi	[56]	MAP	0.242(6)	0.915(3)	4.734(6)
FeGe	[57]	MAP	0.368	1.382	4.787
2D Ising	[58]	Theory	0.125	1.75	15
Mean field	[45]	Theory	0.5	1.0	3.0
3D Heisenberg	[44,59]	Theory	0.365	1.386	4.8
3D XY	[44,60]	Theory	0.345	1.316	4.81
3D Ising	[44,60]	Theory	0.325	1.24	4.82
Tricritical mean field	[61]	Theory	0.25	1.0	5

We also employed DFT simulation to reach a better understanding of magnetism in FeTa$_3$S$_6$. We found the spin magnetic moment is ($\sim$3.65 μ_B) per Fe, indicating that Fe in the FeTa$_3$S$_6$ system behaves as Fe^{+2} [51]. While examining the geometrical structure of the FeTa$_3$S$_6$ system in (Fig. S1b in the Supplemental Material [37]), we realized that the local symmetry of the intercalated Fe^{+2} is D_{3d}, implying that FeS$_6$ octahedron is trigonally distorted. Because of the modification of symmetry $O_h \rightarrow D_{3d}$ symmetry, the 3d orbitals split (see Figs. S1a and S1b in the Supplemental Material [37]), with total spin of $S = 2$, the electronic configuration of the Fe^{+2} is $3d_\uparrow^5(e_g^\pi)_\downarrow^1$, giving the spin magnetic moment $M_{spin} \sim 4\mu_B$. Interestingly, there exists a large orbital magnetic moment($\sim$0.11μ_B) as shown in Fig. 9(a) at the intercalated Fe site. The estimated order of M_{orb}/M_{spin} is $\sim$3%. The spin and orbital magnetic moments have the same sign, indicating that they are coupled parallel. This reflects the fact that the $d-$orbital is more than half-filled. The net magnetic moment $M = M_{spin} + M_{orb}$ thus becomes $\sim$3.76 μ_B, which is consistent with our experimental results of 4.03μ_B.

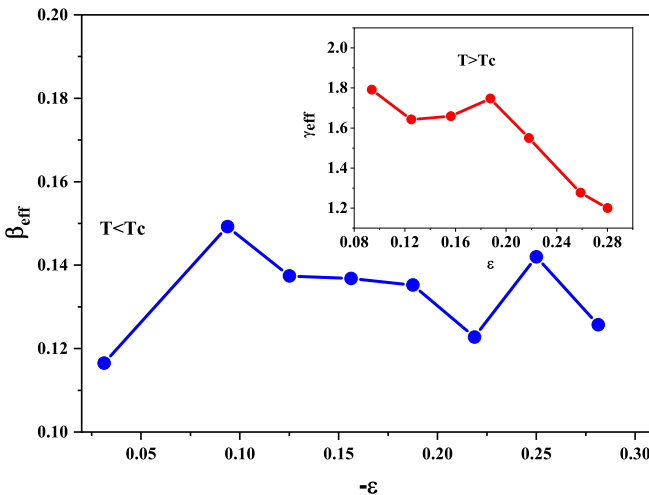Magnetic crystalline anisotropy energy (MAE), in addition to Curie temperature and magnetization strength, is the third most important parameter that characterizes ferromagnetic materials. The MAE can be defined as; MAE $\equiv E(\theta) - E(\perp c)$, where θ is measured from the c axis. MAE based on the noncollinear SOC in Fig. 9(b) shows that the energy of the FeTa$_3$S$_6$ system is gradually growing when all the spin moments are tilting away from the c axis, indicating that the easy axis of the FeTa$_3$S$_3$ system is parallel to the c axis, i.e., $E(\parallel c) < E(\perp c)$. The strength of the MAE is found to be $\sim$3.65 meV per FeTa$_3$S$_6$, which is much higher than other ferromagnetic systems in the same family, such as CrNb$_3$S$_6$, MnNb$_3$S$_6$, and FeNb$_3$S$_6$, and also higher than CrI$_3$ and CrGeTe$_3$ ferromagnetic semiconductors [52–54]. The calculated higher value of MAE hints that there is a strong coupling of spin moments with the c axis, endorsing Ising type behavior as observed in our experimental findings.

Why does FeTa$_3$S$_6$ have such high magnetic anisotropy compared to other ferromagnetic members of the same family, such as CrNb$_3$S$_6$ and MnNb$_3$S$_6$? In principle, the MAE depends on not only the SOC strength of the intercalated magnetic components but also the other factors, which can be seen from the Eq. (7) [52]:

$$E(m) = E_0 + \sum_{i,j} g_i(i - g_j)\frac{H_{ij}}{\epsilon_i - \epsilon_j}\delta_{k_i k_j}$$

$$H_{ij} = \left| < i \mid H_{SO}^{Fe} j > \right|^2 + \left| < i \mid H_{SO}^{Ta} \mid j > \right|^2$$
$$+ < i \mid H_m^{Fe} \mid j >< i \mid H_m^{Ta} \mid j > + c.c. \quad (7)$$

Thus comparatively high MAE in the FeTa$_3$S$_6$ could be due to the following reasons: (i) Fe has a high SOC than Cr and Mn due to its sizable atomic number Z. (ii) In principle, the MAE also depends on the SOC of the host lattice, and therefore Ta based has stronger SOC effects than Nb based transition metal dichalcogenides that is $\lambda_{Nb} \sim 107$ meV and $\lambda_{Ta} \sim 417$ meV, where λ represents the SOC strength. (iii) There exists a $Fe - Ta$ coupling, which can be seen from the density of states (see Figs. S1d and S1i in the Supplemental Material [37]), which also enhances the MAE in the FeTa$_3$S$_6$ system. (iv) The orbital magnetic moment of Fe in the intercalated systems TaS$_2$ and NbS$_2$ are larger by order of magnitude than that of the Mn and Cr. Thus the large orbital magnetic moment in the FeTa$_3$S$_6$ could also be the factor for large MAE in this system compared to other systems belonging to the
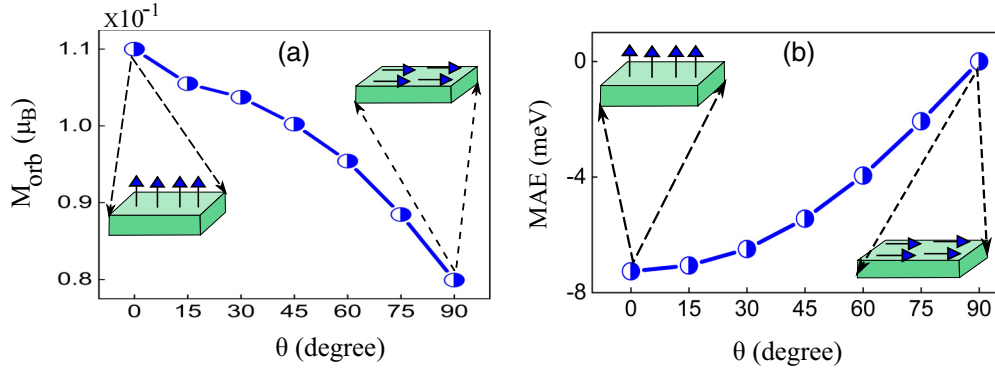

FIG. 8. Effective exponents β_{eff} and γ_{eff} (inset) as a function of reduced temperature ϵ.

FIG. 9. (a) The variation of the orbital magnetic moment $M_{\mathrm{orb}}(\theta)$ as a function of angle θ, where the moderate variation can be observed as spin moments moves from the easy axis ($\parallel c$) to the hard axis ($\perp c$). (b) The magnetic anisotropy, as defined $MAE \equiv E(\theta) - E(\perp c)$, is plotted against different angle θ, where the spin moments being adjusted gradually at different angles measured from the c axis, the $E(\parallel c) < E(\perp c)$ can be noticed.

same family. Furthermore, the origin of out-of-plane magnetic anisotropy ($\parallel c$) in the FeTa$_3$S$_6$ system is investigated by examining the density of states of the FeTa$_3$S$_6$ around the Fermi surface. MAE is expressed in terms of spin-conserving $\Delta S_z = 0$ (also called the spin diagonal process) and spin-flipping $\Delta S_z = 1$ (spin off-diagonal process) processes as MAE $\approx \Delta E^{\downarrow\downarrow} + \Delta E^{\uparrow\uparrow}$ [55], where $\Delta E^{\downarrow\downarrow}[\equiv E^{\downarrow\downarrow}(x) - E^{\downarrow\downarrow}(z)]$ represents the contribution in the MAE due to coupling between spin-down states, and $\Delta E^{\uparrow\downarrow}[\equiv E^{\uparrow\downarrow}(x) - E^{\uparrow\downarrow}(z)]$ represents the coupling between filled spin-up and empty spin-down states. As can be seen from the PDOS (see Fig. S1i in the Supplemental Material [37]), the states around the Fermi level are composed of spin down characters. the spin-flipping process has a small contribution to MAE in our case, and the dominant contribution is coming from the spin-conserving process, which is in principle favour out-of-plane MAE ($\parallel c$), and thus the overall MAE is out-of-plane in the FeTa$_3$S$_6$ systems, ultimately consists with our DFT and experimental findings.

E. Spin interaction in FeTa$_3$S$_6$

For a homogeneous magnet, the universality class of the magnetic phase transition depends on the exchange interaction $J(r)$. Ghosh *et al.* [62] and Fisher *et al.* [63] treated theoretically this type of magnetic coupling as an attractive spin interaction that decays in d-dimension as $J(r) \sim r^{-(d+\sigma)}$, where r and σ are distance and range of interaction, respectively. According to this model, spin interactions are long- or short range, depending on $\sigma < 2$ and $\sigma > 2$, respectively, and it predicts susceptibility exponent γ as follows:

$$\gamma = 1 + \frac{4}{d}\left(\frac{n+2}{n+8}\right)\Delta\sigma + \frac{8(n+2)(n-4)}{d^2(n+8)^2}$$

$$\times \left[1 + \frac{2G\left(\frac{d}{2}\right)(7n+20)}{(n-4)(n+8)}\right]\Delta\sigma^2 \qquad (8)$$

where $\Delta\sigma = (\sigma - \frac{d}{2})$, $G(\frac{d}{2}) = 3 - \frac{1}{4}(\frac{d}{2})^2$, and n represents the spin dimensionality. In order to determine spin dimensionality (n) and lattice dimensionality (d) as well as the range of interactions in FeTa$_3$S$_6$, a procedure similar to Ref. [64] was adopted. In the expression above, the σ parameter is adjusted

for specific values of $\{d : n\}$ such that it produces a value of γ similar to that experimentally observed, $\gamma = 1.423(3)$.

The σ obtained was then used to calculate the other exponents using the following relations: $v = \gamma/\sigma$, $\alpha = 2 - vd$, $\beta = (2 - \alpha - \gamma)/2$, and $\delta = 1 + \gamma/\beta$. The procedure was performed for a different set of $\{d : n\}$. It has been found that for $\{d : n\} = \{2 : 1\}$ and $\sigma = 1.581$, it yields the exponents $\beta = 0.228(2)$, $\gamma = 1.722(3)$, and $\delta = 8.607(1)$, which are well consistent to our experimentally observed values as listed in (Table I). Therefore, the calculations indicate that the spin interaction of 2D Ising type in FeTa$_3$S$_6$ coupled with long-range ($\sigma = 1.581$) interaction.

F. Confirmation of scaling law

In order to ensure the reliability of these critical exponents as well as T_c, it is important to check whether these critical exponents generate the magnetic equation of state for this system in the asymptotic critical region, which is given as follows [45]:

$$M(H, \varepsilon) = \varepsilon^\beta f_\pm(H/\varepsilon^{\beta+\gamma}), \qquad (9)$$

where f_+ ($T > T_c$) and f_- ($T < T_c$) are the regular functions. Furthermore, Eq. (9) can be expressed in terms of renormalized magnetization $m = M(H, \epsilon)\epsilon^{-\beta}$ and renormalized field $h = H\epsilon^{-(\beta+\gamma)}$ as

$$m = f_\pm h. \qquad (10)$$

Equation (10) indicates that for the correct choice of critical exponents m vs h should form two universal curves above and below T_c, respectively, even in the low-field regions [65,66]. However, the scaling becomes divergent at the boundary between the phases if a field-induced phase transition occurs. The divergence of the scaling curves provided a mechanism to differentiate the various phases [56]. Figure 10(a) shows the plot of the isothermal magnetization based on the scaling equation around the critical temperature, while the inset of Fig. 10(a) shows the same plot on log-log scale. It has been observed that the $m(h)$ curves above T_c are collapsing into a single branch well, but those below T_c are slightly dispersed in the low-field region. The dispersion is clearly visible in
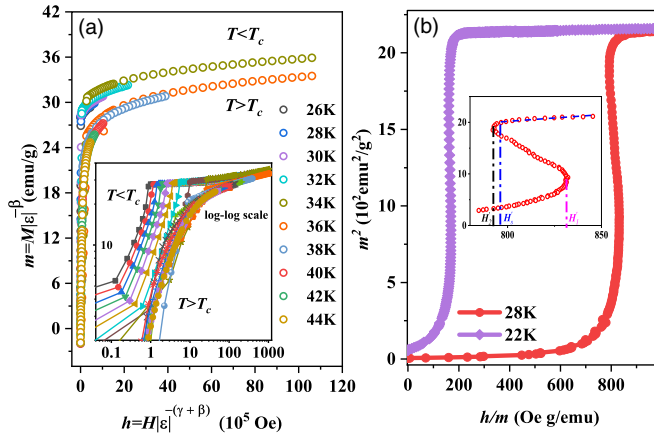
FIG. 10. (a) scaling plots around T_c using β and γ determined by the modified Arrott plot analysis; (b) rescaled of m^2 vs h/m at 24 K and 28 K. The inset shows the magnified regions correspond to H_1', H_2', and H_s' (definitions of H_1' and H_2' and H_s' are given in the text).

the $m(h)$ curve [following Eq. (10)] plotted on the log-log scale as shown in the inset of Fig. 10(a) in low-field regions. The low-field dispersion in the scaled curves and the corresponding phase transitions have been further ensured with a more rigorous method by plotting m^2 vs h/m, as shown in Fig. 10(b). The S-shaped m^2 vs h/m curves at selected temperatures below T_c in Fig. 10(b) indicates three distinguishable regions or phases (P), a low-field platform (P_1), a sudden increase with a negative slope (P_2) and a change in the sign of slope and then saturates (P_3). The three inflection points are marked as H_1', H_2', and H_s'. The phase transition process observed in the scaling curves is identical to that observed in the $d[M(H)]/dH$ curves and the field values H_1', H_2', and H_s' that induce these transitions are correspond very well to H_1, H_2, and H_s.

G. Phase diagram

FeTa$_3$S$_6$ and its isostructural solids belonging to the space group $P6_322$ (chiral and noncentrosymmetric characteristics), such as MnNb$_3$S$_6$ and CrNb$_3$S$_6$, demonstrate the trend in the formation of the ordered magnetic compound. In principle, the Dzyaloshinskii-Moriya (DM) interaction could not be ignored owing to the lack of inversion symmetry in these compounds. These systems also exhibit strong magnetic crystalline anisotropy (MCA) either along or perpendicular to the c axis, depending on the type of intercalated magnetic component in these systems. The interplay between the so-called anisotropic exchange interaction (i.e., DM interaction) and the MCA will decide the ground magnetic state of these systems. For instance, if the DM dominates MCA interactions, the system will typically reside in the HM state. In contrast, the system will otherwise be collinear magnetic. However, an applied external magnetic field or strengthening MCA in these systems leads to the phase transition from the so-called noncollinear (HM) state to the collinear ferromagnetic state.

P_1 is unambiguously attributed to the HM phase as a result of competition between DM interaction and magnetic exchange interaction in FeTa$_3$S$_6$. The HM ordering is usually modulated into novel and exotic phases, for example,
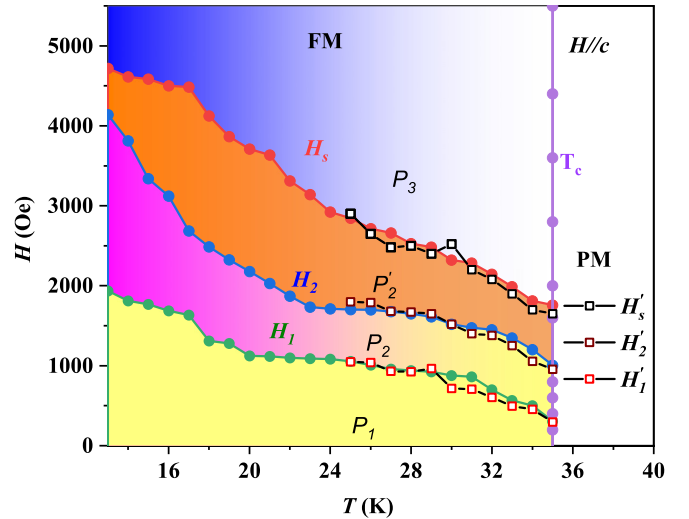

FIG. 11. $H - T$ phase diagram in the vicinity of the phase transition for FeTa$_3$S$_6$ with $H \parallel c$. P_1, P_2, P_2', and P_3 phases are explained in the text; symbols H_1, H_2, and H_s are obtained from $M(H)$ curves and H_1', H_2', and H_s' obtained from critical scaling.

particle-like spin textures, including a skyrmion and a magnetic soliton, if an external magnetic field is applied above a threshold value. The phenomenon has already been observed in isostructural HM systems CrNb$_3$S$_6$. From this analogy the low-field induced phase (P_2) above inflection point H_1' in FeTa$_3$S$_6$ is field modulated exotic magnetic phase. The transition from the (P_2) to the (P_3) phase is due to the competition between the (P_2) and the FM. In the lower-field region, the (P_2) is dominant and separated from the FM region. In the higher-field region, the FM phase becomes dominant in the system where the whole magnetization is very close to the FM behavior (P_2'), and the critical field from P_2 to (P_2') is defined as H_2'. Whereas above the inflection point H_s', P_3 is a field-induced FM phase. The threshold field H_s' is needed at any specific temperature to strengthen MCA against DM to realize a collinear FM phase in FeTa$_3$S$_6$. The detailed $H - T$ phase diagram based on $M(H)$, $d[M(H)]/dH$, and scaling curves for $H \parallel c$ is shown in Fig. 11.

III. CONCLUSIONS

In summary, we conducted a comprehensive study of magnetism in the quasi-2D ferromagnet FeTa$_3$S$_6$. The direction dependent magnetization revealed a strong magnetic anisotropy along the geometrical c axis ($H \parallel c$) in FeTa$_3$S$_6$. The estimated out-of-plane magnetic anisotropy energy (MAE) is $\sim$3.65 meV per FeTa$_3$S$_6$ as determined by our first-principle simulation, in complete agreement with our experimental findings. The (PM-FM) phase transition around 35 K is identified to be the second order in nature. The critical behavior analysis around PM-FM transition yields critical exponents $\beta = 0.189(2)$, $\gamma = 1.423(1)$, and $\delta = 8.531(7)$. At high field for ($H > H_s$), the estimated critical exponents follow the scaling equation, ensuring that the exponents obtained are unambiguous and intrinsic to the material. The obtained exponents match well with those deduced from the results of the renormalization group approach for a 2D Ising

($\{d : n\} = \{2 : 1\}$) system coupled with a long-range ($\sigma = 1.581$) interaction. Whereas, at the low fields, the divergence in the scaling curves suggest field induced phase transition in FeTa$_3$S$_6$. Based on the universality scaling, $M(H)$ and $d[M(H)]/dH$ the $H - T$ phase diagram was constructed. On the other hand, in supporting experimental results via DFT simulation, we explain the magnetic picture, such as the origin of higher MAE and its out-of-plane existence. Our presented physical insights for FeTa$_3$S$_6$ could be useful to understand the macroscopic magnetic picture in materials referring to TMDCs being intercalated with transition metals.

[1] Q. H. Wang, K. Kalantar-Zadeh, A. Kis, J. N. Coleman, and M. S. Strano, Nat. Nanotechnol. **7**, 699 (2012).

[2] A. K. Geim and I. V. Grigorieva, Nature (London) **499**, 419 (2013).

[3] S. Lebègue, T. Björkman, M. Klintenberg, R. M. Nieminen, and O. Eriksson, Phys. Rev. X **3**, 031002 (2013).

[4] C. Gong, L. Li, Z. Li, H. Ji, A. Stern, Y. Xia, T. Cao, W. Bao, C. Wang, Y. Wang *et al.*, Nature (London) **546**, 265 (2017).

[5] H. Ji, R. A. Stokes, L. D. Alegria, E. C. Blomberg, M. A. Tanatar, A. Reijnders, L. M. Schoop, T. Liang, R. Prozorov, K. S. Burch *et al.*, J. Appl. Phys. **114**, 114907 (2013).

[6] B. Sachs, T. O. Wehling, K. S. Novoselov, A. I. Lichtenstein, and M. I. Katsnelson, Phys. Rev. B **88**, 201402(R) (2013).

[7] I. Yamada, J. Phys. Soc. Jpn. **33**, 979 (1972).

[8] H. Kabbour, R. David, A. Pautrat, H.-J. Koo, M.-H. Whangbo, G. André, and O. Mentré, Angew. Chem., Int. Ed. **51**, 11745 (2012).

[9] M. A. McGuire, H. Dixit, V. R. Cooper, and B. C. Sales, Chem. Mater. **27**, 612 (2015).

[10] L. D. Casto, A. J. Clune, M. O. Yokosuk, J. L. Musfeldt, T. J. Williams, H. L. Zhuang, M.-W. Lin, K. Xiao, R. G. Hennig, B. C. Sales *et al.*, APL Mater. **3**, 041515 (2015).

[11] X. Zhang, Y. Zhao, Q. Song, S. Jia, J. Shi, and W. Han, Jpn. J. Appl. Phys. **55**, 033001 (2016).

[12] J. L. Miller, Phys. Today **70**, 16 (2017).

[13] Z. Wang, M. Gibertini, D. Dumcenco, T. Taniguchi, K. Watanabe, E. Giannini, and A. F. Morpurgo, Nat. Nanotechnol. **14**, 1116 (2019).

[14] D. Ghazaryan, M. T. Greenaway, Z. Wang, V. H. Guarochico-Moreira, I. J. Vera-Marun, J. Yin, Y. Liao, S. V. Morozov, O. Kristanovski, A. I. Lichtenstein *et al.*, Nat. Electron. **1**, 344 (2018).

[15] W. Chen, Z. Sun, Z. Wang, L. Gu, X. Xu, S. Wu, and C. Gao, Science **366**, 983 (2019).

[16] Z. Wang, T. Zhang, M. Ding, B. Dong, Y. Li, M. Chen, X. Li, J. Huang, H. Wang, X. Zhao *et al.*, Nat. Nanotechnol. **13**, 554 (2018).

[17] Y. Deng, Y. Yu, Y. Song, J. Zhang, N. Z. Wang, Z. Sun, Y. Yi, Y. Z. Wu, S. Wu, J. Zhu *et al.*, Nature (London) **563**, 94 (2018).

[18] Z. Fei, B. Huang, P. Malinowski, W. Wang, T. Song, J. Sanchez, W. Yao, D. Xiao, X. Zhu, A. F. May *et al.*, Nat. Mater. **17**, 778 (2018).

[19] Z. Wang, I. Gutiérrez-Lezama, N. Ubrig, M. Kroner, M. Gibertini, T. Taniguchi, K. Watanabe, A. Imamoğlu, E. Giannini, and A. F. Morpurgo, Nat. Commun. **9**, 2516 (2018).

[20] Z. Ma, W. Zhu, G. Lin, Y. Liu, F. Jin, Y. Yang, T. Wu, X. Luo, Y. Sun, J. Chen *et al.*, AIP Adv. **9**, 125116 (2019).

[21] N. D. Mermin and H. Wagner, Phys. Rev. Lett. **17**, 1133 (1966).

[22] B. Huang, G. Clark, D. R. Klein, D. MacNeill, E. Navarro-Moratalla, K. L. Seyler, N. Wilson, M. A. McGuire, D. H. Cobden, D. Xiao *et al.*, Nat. Nanotechnol. **13**, 544 (2018).

[23] J. Su, M. Wang, G. Liu, H. Li, J. Han, and T. Zhai, Adv. Sci. **7**, 2001722 (2020).

[24] M. Eibschütz, S. Mahajan, F. J. DiSalvo, G. W. Hull, and J. V. Waszczak, J. Appl. Phys. **52**, 2098 (1981).

[25] P. E. Blöchl, Phys. Rev. B **50**, 17953 (1994).

[26] G. Kresse and J. Furthmüller, Phys. Rev. B **54**, 11169 (1996).

[27] J. P. Perdew, J. A. Chevary, S. H. Vosko, K. A. Jackson, M. R. Pederson, D. J. Singh, and C. Fiolhais, Phys. Rev. B **48**, 4978(E) (1993).

[28] A. I. Liechtenstein, V. I. Anisimov, and J. Zaanen, Phys. Rev. B **52**, R5467 (1995).

[29] K.-T. Ko, K. Kim, S. B. Kim, H.-D. Kim, J.-Y. Kim, B. I. Min, J.-H. Park, F.-H. Chang, H.-J. Lin, A. Tanaka, and S.-W. Cheong, Phys. Rev. Lett. **107**, 247201 (2011).

[30] S. Grimme, J. Antony, S. Ehrlich, and H. Krieg, J. Chem. Phys. **132**, 154104 (2010).

[31] E. Morosan, H. W. Zandbergen, L. Li, M. Lee, J. G. Checkelsky, M. Heinrich, T. Siegrist, N. P. Ong, and R. J. Cava, Phys. Rev. B **75**, 104401 (2007).

[32] J. G. Checkelsky, M. Lee, E. Morosan, R. J. Cava, and N. P. Ong, Phys. Rev. B **77**, 014433 (2008).

[33] H. Han, L. Zhang, D. Sapkota, N. Hao, L. Ling, H. Du, L. Pi, C. Zhang, D. G. Mandrus, and Y. Zhang, Phys. Rev. B **96**, 094439 (2017).

[34] Y. Dai, W. Liu, Y. Wang, J. Fan, L. Pi, L. Zhang, and Y. Zhang, J. Phys.: Condens. Matter **31**, 195803 (2019).

[35] D. Obeysekera, K. Gamage, Y. Gao, S.-w. Cheong, and J. Yang, Adv. Electron. Mater. **7**, 2100424 (2021).

[36] S. Fan, I. Manuel, A. al-Wahish, K. R. O'Neal, K. A. Smith, C. J. Won, J. W. Kim, S.-W. Cheong, J. T. Haraldsen, and J. L. Musfeldt, Phys. Rev. B **96**, 205119 (2017).

[37] See Supplemental Material at http://link.aps.org/supplemental/10.1103/PhysRevB.105.144413 for the theoretical analysis, source of magnetism, and origin of magnetic anisotropy.

[38] G. Zheng, M. Wang, X. Zhu, C. Tan, J. Wang, S. Albarakati, N. Aloufi, M. Algarni, L. Farrar, M. Wu *et al.*, Nat. Commun. **12**, 1 (2021).

[39] N. J. Ghimire, M. A. McGuire, D. S. Parker, B. Sipos, S. Tang, J.-Q. Yan, B. C. Sales, and D. Mandrus, Phys. Rev. B **87**, 104403 (2013).

[40] E. M. Clements, R. Das, L. Li, P. J. Lampen-Kelley, M.-H. Phan, V. Keppens, D. Mandrus, and H. Srikanth, Sci. Rep. **7**, 6545 (2017).

[41] Y. Kousaka, T. Ogura, J. Zhang, P. Miao, S. Lee, S. Torii, T. Kamiyama, J. Campo, K. Inoue, and J. Akimitsu, J. Phys.: Conf. Ser. **746**, 012061 (2016).

[42] Y. Kousaka, Y. Nakao, J. Kishine, M. Akita, K. Inoue, and J. Akimitsu, Nucl. Instrum. Methods Phys. Res., Sect. A **600**, 250 (2009).

[43] S. K. Karna, F. N. Womack, R. Chapai, D. P. Young, M. Marshall, W. Xie, D. Graf, Y. Wu, H. Cao, L. DeBeer-Schmitt, P. W. Adams, R. Jin, and J. F. DiTusa, Phys. Rev. B **100**, 184413 (2019).

[44] B. Banerjee, Phys. Lett. **12**, 16 (1964).

[45] H. E. Stanley, *Phase Transitions and Critical Phenomena* (Clarendon Press, Oxford, 1971).

[46] A. Arrott and J. E. Noakes, Phys. Rev. Lett. **19**, 786 (1967).

[47] A. K. Pramanik and A. Banerjee, Phys. Rev. B **79**, 214426 (2009).

[48] B. Widom, J. Chem. Phys. **43**, 3892 (1965).

[49] J. Mira, J. Rivas, M. Vázquez, J. M. García-Beneytez, J. Arcas, R. D. Sánchez, and M. A. Señarís Rodríguez, Phys. Rev. B **59**, 123 (1999).

[50] L. Zhang, B. Wang, Y. Sun, P. Tong, J. Fan, C. Zhang, L. Pi, and Y. Zhang, Phys. Rev. B **85**, 104419 (2012).

[51] J. Dijkstra, P. J. Zijlema, C. F. van Bruggen, C. Haas, and R. A. de Groot, J. Phys.: Condens. Matter **1**, 6363 (1989).

[52] M. Mito, H. Ohsumi, T. Shishidou, F. Kuroda, M. Weinert, K. Tsuruta, Y. Kotani, T. Nakamura, Y. Togawa, J. Kishine, Y. Kousaka, J. Akimitsu, and K. Inoue, Phys. Rev. B **99**, 174439 (2019).

[53] S. Mankovsky, S. Polesya, H. Ebert, and W. Bensch, Phys. Rev. B **94**, 184430 (2016).

[54] L. Webster and J.-A. Yan, Phys. Rev. B **98**, 144411 (2018).

[55] D.-s. Wang, R. Wu, and A. J. Freeman, Phys. Rev. B **47**, 14932 (1993).

[56] L. Zhang, D. Menzel, C. Jin, H. Du, M. Ge, C. Zhang, L. Pi, M. Tian, and Y. Zhang, Phys. Rev. B **91**, 024403 (2015).

[57] H. Wilhelm, A. O. Leonov, U. K. Rößler, P. Burger, F. Hardy, C. Meingast, M. E. Gruner, W. Schnelle, M. Schmidt, and M. Baenitz, Phys. Rev. B **94**, 144424 (2016).

[58] A. Rahman, M. u. Rehman, D. Zhang, M. Zhang, X. Wang, R. Dai, Z. Wang, X. Tao, L. Zhang, and Z. Zhang, Phys. Rev. B **100**, 214419 (2019).

[59] M. Campostrini, M. Hasenbusch, A. Pelissetto, P. Rossi, and E. Vicari, Phys. Rev. B **65**, 144520 (2002).

[60] J. C. Le Guillou and J. Zinn-Justin, Phys. Rev. B **21**, 3976 (1980).

[61] S. J. Poon and J. Durand, Phys. Rev. B **16**, 316 (1977).

[62] K. Ghosh, C. J. Lobb, R. L. Greene, S. G. Karabashev, D. A. Shulyatev, A. A. Arsenov, and Y. Mukovskii, Phys. Rev. Lett. **81**, 4740 (1998).

[63] M. E. Fisher, S.-k. Ma, and B. G. Nickel, Phys. Rev. Lett. **29**, 917 (1972).

[64] S. F. Fischer, S. N. Kaul, and H. Kronmüller, Phys. Rev. B **65**, 064443 (2002).

[65] M. Phan, V. Franco, N. Bingham, H. Srikanth, N. Hur, and S. Yu, J. Alloys Compd. **508**, 238 (2010).

[66] N. Khan, A. Midya, K. Mydeen, P. Mandal, A. Loidl, and D. Prabhakaran, Phys. Rev. B **82**, 064422 (2010).